A multiphoton ionization study of the photodissociation dynamics of the S_2 state of CH_3ONO

J. W. Winniczek
Department of Chemistry, Brookhaven National Laboratory, Upton, New York 11973

R. L. Dubs
Arthur Amos Noyes Laboratory of Chemical Physics,[a] California Institute of Technology, Pasadena, California 91125

J. R. Appling[b]
Department of Chemistry, Brookhaven National Laboratory, Upton, New York 11793

V. McKoy
Arthur Amos Noyes Laboratory of Chemical Physics,[a] California Institute of Technology, Pasadena, California 91125

M. G. White
Department of Chemistry, Brookhaven National Laboratory, Upton, New York 11793

(Received 1 August 1988; accepted 14 October 1988)

Two-color (1 + 1) REMPI (resonantly enhanced multiphoton ionization) photoelectron spectroscopy is used to probe the NO photofragments produced by the UV photodissociation of methyl nitrite, i.e., $CH_3ONO + h\nu \rightarrow CH_3ONO^*(S_2) \rightarrow CH_3O\cdot(X) + NO(X, v, J)$. The photofragments are produced in their ground electronic states but with high rotational and translational energy. NO fragment angular distributions, rotational state distributions, and spatial alignment are determined by photoion and photoelectron detection. The initial state alignment is obtained by the CDAD (circularly dichroic angular distribution) technique for the first time. CDAD measurements for rotational levels with $35.5 \leqslant J \leqslant 46.5$ result in alignment parameters at the classical high-J limit of $\mathscr{A}_0^{(2)} = -0.4$. This alignment is consistent with an "impulsive" dissociation mechanism in which photofragment recoil along the CH_3O–NO bond imparts substantial rotational angular momentum to the NO molecule resulting in a high-J state distribution and preferential rotation in the plane of dissociation. These measurements clearly establish the utility of the CDAD method for probing chemical processes in which spatial alignment plays an important role. Photoion angular distributions are used to probe correlations between the CH_3ONO transition dipole moment, NO fragment velocity, and angular momentum. These correlations reveal additional details of the photolysis mechanism.

I. INTRODUCTION

Photodissociation processes which yield NO as a fragment have been the subject of numerous investigations.[1] The NO fragment has been chosen for detailed study on the basis of its well defined spectroscopy and the accessibility of its excited states with current laser technology. A number of groups have been conducted detailed studies of several representative molecules, such as: nitrous acid, HONO,[2,3] methyl nitrite, CH_3ONO,[4–13] ethyl nitrite,[14,15] and t-butyl nitrite, $(CH_3)_3CONO$.[16,17] These studies probed the angular distributions, vibrational and rotational energy distributions, and alignment of the NO product fragment. The dissociation was achieved by exciting either of two lowest states common to all of the abovementioned species. The S_1 state is characterized by a structured $\pi^* \leftarrow n$ band in the range 300–380 nm; only vibrational structure is clearly discernible, suggesting that this is a short-lived predissociative state. The S_2 state is associated with a structureless broad $\pi^* \leftarrow \pi$ absorption band in the range 180–250 nm, characteristic of a purely repulsive state. For both of these dissociation channels the NO is produced in its lowest electronic state ($X\,^2\Pi$), with small vibrational excitation and high rotational and translational energy. Since the S_1 and S_2 states appear to involve very different dissociation mechanisms, investigations of the alkyl nitrites are extremely useful for probing a wide range of dynamical interactions responsible for the dissociation of polyatomic molecules.

The predominant tool used to probe detailed dynamics of dissociation is laser induced fluorescence (LIF) with Doppler line shape analysis.[18–20] The line shape and intensity are a function of the velocity and alignment of the photofragment, as well as the angular correlation between the angular momentum, the dissociation dipole moment, and velocity vectors. Variations in geometrical arrangement of dissociation and excitation lasers and fluorescence detector selectively bring out these dynamical features. The requirement for probing fragments with LIF is that the fragment have a significant fluorescence signal, a condition which cannot be realized for many molecules. Resonantly enhanced multiphoton ionization (REMPI) is generally considered to provide greater sensitivity than LIF for detecting the expected low concentrations of photolysis products, in addition to

[a] Contribution No. 7812.
[b] Present address: Department of Chemistry, University of Kentucky, Lexington, KY 40506-0055.

 0021-9606/89/020949-15$02.10

having a wider applicability.[21,22] Theoretical formulations have been developed that permit extraction of alignment information from REMPI data, independently of the ionization dynamics.[23–28] Recently, experimental verification of this technique has been made in the analysis of photon-induced alignment of free NO.[29] In these experiments circularly dichroic angular distributions (CDAD) of photoelectrons are measured and the alignment is extracted by way of relatively simple mathematical relations. Application of the CDAD technique to the determination of *ground* state alignment induced by photodissociation is presented here for the first time.

The thrust of the work presented in this paper is to investigate the dissociation of the S_2 state of CH_3ONO as well as to demonstrate the utility of the CDAD technique[23–28] in photodissociation studies. As part of this endeavor, we also introduce a method for analysis of vector correlations in photodissociation by measuring the angular distribution of REMPI photoions.

II. EXPERIMENTAL

Photoelectron angular distribution, dissociation product angular distribution, and rotational state population distribution measurements were performed on a photoelectron spectrometer system which has been described in previous publications.[29,30] The system consists of a time-of-flight photoelectron/ion spectrometer in a vacuum chamber, and pulsed laser light sources of dissociation, excitation, and probe radiation. The time-of-flight spectrometer samples electrons or ions along an axis which is perpendicular to an axis defined by two windows in the vacuum chamber. One of the windows admits tunable linearly polarized laser radiation; the polarization vector is rotated with a Soleil–Babinet compensator tuned to 1/2-wave retardation at the wavelength of interest. The other window admits 266 nm radiation coaxially to the tunable light. The 266 nm light can be right circularly polarized, left circularly polarized, or linearly polarized by rotating the axis of a 1/4-wave plate at an angle of 45°, −45°, or 0°, respectively, from the incoming polarization vector. Both light beams are focused through 250 mm lenses mounted on translation stages to allow adjustable beam overlap. The focus is adjusted to maximize signal for two-color (1 + 1′) REMPI, and to reduce one-color (tunable light) (1 + 1) REMPI.

The laser system consists of a pulsed (20 Hz) Nd:YAG (Quanta Ray DCR-2A) laser producing IR and 532 nm light with 2–3 ns pulse widths. The 532 nm photons pump a tunable dye laser (Quanta Ray PDL-1) using an approximately 6:1 mix of R590 and R610 laser dyes (Exciton). The output of the dye laser is doubled (Quanta Ray WEX), and is then mixed with residual IR to produce tunable UV radiation in the range of 227 to 223 nm with 1.0 to 2.0 mJ/pulse. A 10% beam splitter diverts some of the 532 nm pump beam to a frequency doubling crystal which produces the 266 nm light at 5 mJ/pulse. The 266 nm light can be temporally delayed 3–30 ns by extending its path length.

The methyl nitrite is synthesized[31] by slow addition of an acidic solution of nitrosylsulfuric acid ($HOSO_2ONO$) to water-diluted methanol (CH_3OH) under a slow flow of helium. The product is purified by trap (dry-ice–acetone bath temperature) to trap (liquid nitrogen temperature) distillation. In a dry-ice–acetone bath, the CH_3ONO has a vapor pressure of a several Torr; it can therefore be introduced into the vacuum chamber via an effusive inlet regulated with an automatic leak valve, to give an operating pressure 7×10^{-5} Torr. A pulsed valve inlet was not used since decomposition and clustering were difficult to control.

Photoelectron angular distributions (CDAD) are measured for the left and right circularly polarized probe laser (266 nm) as two distinct angular spectra, in which the polarization angle (relative to the detector axis) of the tunable light is scanned from 90° to 270° in increments of 10°. The scan is repeated 16 times per spectrum with 60 laser shots per angle each time. A photodiode triggered by the tunable laser light initiates the TOF digitizer. The tunable radiation performs two functions: the dissociation of the CH_3ONO via the S_2 state and excitation of the product NO from the $X\,^2\Pi$, $v=0$ state to the $A\,^2\Sigma$, $v=0$ state. Since the S_2 state is very broad and featureless,[32] the absorption curve of CH_3ONO can be regarded as being flat. The TOF photoelectron spectrum may show two (1 + 1) REMPI peaks: a fast (~1.8 eV) one-color peak due to 227–223 nm ionization and a slower (~0.9 eV) two-color peak due to 266 nm ionization. The two-color process is selected by integrating the slower peak for each shot of the laser; the unwanted one-color signal is also reduced to below 1% of that for the two color by adjusting the focus of both laser beams. Methyl nitrite can also be dissociated by the 266 nm light. This unwanted process was eliminated by delaying the 266 nm light relative to the 223–227 nm radiation 12 ns, permitting the CH_3ONO to dissociate and the product NO to be excited while the 266 nm ionizing (probe) laser is off. The delayed 266 nm pulse then ionizes these excited NO fragments but cannot directly ionize ground state NO photofragments produced by 266 nm induced fragmentation.

Wavelength spectra are collected in the magic angle PINDAD configuration (MAP—the polarization-into-detector angular distribution technique is described in Sec. III B): the 1/4-wave plate is set at 0° to yield linearly polarized 266 nm radiation, with the polarization vector along (into) the detector axis. The tunable light polarization is set at the "magic angle", 54.7° from the detector axis. In order to reduce long term instabilities and effects of laser position drift with wavelength, spectra were collected in 0.62 nm wide regions with 20% overlap between regions. The dye laser was stepped linearly by 0.0048 nm steps of its output wavelength λ_{dl} [the doubled and summed wavelength is $\lambda=(2/\lambda_{dl}+1/1064)^{-1}$ nm]. The spectrum segments were concatenated using the overlap region for intersegment normalization. Along with the photoelectron signal the pulse energy was measured at each wavelength with a Joule meter (Laser Precision RJP-735). The spectra were corrected for power fluctuations; since the dye curve was relatively flat the power corrected spectra did not significantly differ from the uncorrected ones. Each spectrum was scanned once with 200 laser shots per wavelength channel. Several spectra were collected in order to ensure consistency. Heights h of peaks of interest were obtained by fitting each peak to a

Gaussian, $P(\lambda) = h \cdot \exp[-\alpha(\lambda - \lambda_0)^2]$ (the fitted parameters were h, α, and λ_0). The peak heights in conjunction with Eqs. (17)–(19) were used to extract rotational populations, as will be discussed below.

Ion angular distributions were obtained with the TOF spectrometer by changing the voltage potentials on various elements. The TOF spectrometer is operated in a way that significantly deviates from the space-focusing conditions described by Wiley and McLaren,[33] and a similar approach was used by Ogorzalek-Loo *et al.*[34] This mode of operation permits dispersion of velocities of the NO. When used in photoelectron angular distribution and wavelength measurements the TOF spectrometer is essentially operated as a pure electron drift instrument with all potentials at zero (+ 0.25 V is applied to the Faraday cage flight tube[30]). For the ion studies, a repeller opposite the TOF entrance aperture is set to $\approx$ + 50 V, the entrance aperture is at 0 V, an acceleration of $\approx$ − 80 V is provided into the field-free Faraday cage flight tube. Characteristic features of the TOF spectrum are two broad peaks; the fast one corresponds to NO fragments moving into the detector prior to ionization; the slow one corresponds to fragments initially moving in the opposite direction, away from the detector. (Note that for thermal NO the TOF spectrum exhibits one sharp peak located in the region between the two broad peaks.) The angular resolution for these conditions is $\approx 35°$ (in contrast to $\approx 2°$ for the photoelectron measurements). The probe (ionizing) laser is set for linearly polarized light, the polarization vector along the detector axis. The polarization vector of the probe laser is scanned from 0° to 180° in increments of 10°. The fast TOF peak is integrated over time to generate a data point at a given angle. The scan is repeated eight times per spectrum with 60 laser shots per angle each time.

III. DATA ANALYSIS

A molecule, such as a photolysis fragment, in a rotational state J has $2J + 1$ substates, $M_J = -J, -J + 1, ..., J - 1, J$. If the populations N_{M_J} of these substates M_J are equal then the state is considered to be *isotropic*. If however, substates with different $|M_J|$ values have different populations the state is considered to be *aligned*.[35,36] The populations can be expanded in a "spherical" basis[36]

$$N_{M_J} = \sum_L A_L \, T_L^{M_J}, \tag{1}$$

where the A_L are the multipole moments of alignment. The $T_L^{M_J}$ are known as spherical tensor operators which can be expressed as Clebsch–Gordon coefficients,

$$T_L^{M_J} = (-1)^{J - M_J} \langle J \, J \, M_J - M_J | L \, 0 \rangle.$$

Classically, M_J is the projection of **J** onto an axis at angle α, $M_J = J \cos \alpha$, and the $T_L^{M_J} \propto P_L(\cos \alpha)$ (the P_L are Legendre polynomials of order L).

Two distinct $(n + 1)$ REMPI techniques for obtaining the alignment of gas phase molecules from photoelectron angular distributions have been proposed by Dubs, Dixit, and McKoy.[23–25,27] The first, circular dichroism in angular distributions (CDAD) of photoelectrons, requires that the molecule be excited with n photons of linearly polarized light and ionized with one photon of left or right circularly polarized light. The CDAD spectrum is the difference between left and right angular spectra,[23,26] $I_{\text{CDAD}}(\theta) = I_{\text{left}}(\theta) - I_{\text{right}}(\theta)$, where photoelectron flux is measured as a function of the angle between the polarization of the excitation light and the detector axis. If the excitation and ionization photons propagate along a single line and the photoelectrons are measured in a plane perpendicular to that line, then the CDAD angular spectrum can be expressed as an expansion in associated Legendre polynomials[24,25,27,29]

$$I_{\text{CDAD}}(\theta) = \sum_L a_L \, P_L^1(\cos \theta) \tag{2}$$

with

$$a_L = A_L \bar{\beta}_L, \tag{3}$$

where the $\bar{\beta}_L$ contain the dynamics of the ionization, and the A_L are the multipole moments of the n-photon excited state.

The other alignment probe scheme differs from CDAD in that the ionization step is done by linearly polarized light, with the polarization vector pointing into the detector, hence the name: polarization-into-detector angular distribution, PINDAD.[25] For counterpropagating excitation and ionization lasers, the PINDAD angular spectrum can be expanded in Legendre polynomials[25]

$$I_{\text{PINDAD}}(\theta) = \sum_L a'_L \, P_L(\cos \theta) \tag{4}$$

with

$$a'_L = A_L \beta_L, \tag{5}$$

where the β_L contain the dynamics of the PINDAD ionization,[37] and the A_L are the same as in Eq. (3). Note that only one angular spectrum is required to obtain I_{PINDAD}.

A. CDAD data analysis

A method for the determination of ground state alignment by $(n + 1)$ CDAD has been presented in Refs. 25 and 27. In the method proposed, the ratio of a_2 values [Eq. (2)] from two different branches is experimentally determined and used in a simple formula to extract the ground state alignment. The method suffers from the disadvantage that the a_2 values for two different angular spectra must be determined *relative to one another*. In practice, this means normalizing each a_2 value to be the intensity of the left or right photoelectron spectrum at a particular angle, say 90°, and later taking a wavelength spectrum with the detector fixed at that angle in order to determine the relative a_2 values. While this procedure is certainly feasible, the necessity of a wavelength spectrum is experimentally inconvenient. For this reason, a method of analysis which eliminates this requirement is presented here.

Ideally, the a_2 values from the CDAD angular spectra would be normalizable by some quantity in the CDAD (left or right) angular spectrum which has the same convenient analytical properties as the CDAD coefficients. The most obvious quantity would be a_0, proportional to the excited state populations. Unfortunately, unlike the PINDAD case, a_0 is not analytically obtainable from a CDAD angular spec-

trum.[25] Nevertheless, the area under the left or right angular spectrum is found to be approximately proportional to a_0; the error is calculated to be on the order of 1%–2% over a wide range of initial state alignments.[38] This error is considered to be acceptable for the present purposes. In this regard, it should be pointed out that, while in Ref. 29 (Sec. III C) the intensity of the left or right spectrum at 90°, $I(90°)$, was shown to be approximately related to a_0, this approximation was considered only for P and R branches. Overall, the error in using $I(90°)$ rather than the area as an approximation to a_0 is calculated[38] to be on the order of 10%.

The CDAD a_2 value normalized by the area under the left or right spectrum, labeled $\bar{a}_2$ can now be written as

$$\bar{a}_2 = \frac{a_2}{\text{Area}} \approx \frac{a_2}{a_0} = \frac{A_2 \bar{\beta}_2}{A_0 \bar{\beta}_0}, \tag{6}$$

where A_0 is the excited state population, A_2 is the excited state quadrupole moment, and $\bar{\beta}_0$ and $\bar{\beta}_2$ contain information about the photoionization dynamics. The excited state alignment A_2 can be related to the ground state alignment $\tilde{A}_2$ by [Eq. (5) of Ref. 25]

$$A_L = \sum_{L''} \tilde{A}_{L''} C_{L''L}, \tag{7}$$

$$A_0 = \tilde{A}_0 C_{00} + \tilde{A}_2 C_{20}, \tag{8}$$

$$A_2 = \tilde{A}_0 C_{02} + \tilde{A}_2 C_{22}, \tag{9}$$

where $\tilde{A}_{L''}$ is the ground state alignment. Analytical expressions for the $C_{L''L}$ are given in Table I of Ref. 25.[39] The J' (angular momentum of the excited state) dependence of $\bar{\beta}_L$ in Eq. (6) can be factored out [Eq. (19) of Ref. 25]:

$$\bar{\beta}_L(J') = X_L(J')\tilde{\beta}_L, \tag{10}$$

where $\tilde{\beta}_L$ is explicitly independent of J' and can be treated as a constant.[25] Analytical expressions for X_0 and X_2 are given in Ref. 25 [Eqs. (21) and (22)].

Using Eqs. (8), (9), and (10), Eq. (6) can be written as

$$\bar{a}_2 \propto \frac{[\tilde{A}_0 C_{02} + \tilde{A}_2 C_{22}]\, X_2 \tilde{\beta}_2}{[\tilde{A}_0 C_{00} + \tilde{A}_2 C_{20}]\, X_0 \tilde{\beta}_0}. \tag{11}$$

The alignment parameters $\tilde{A}_0$ and $\tilde{A}_2$ can be related to the parameter $\mathscr{A}_0^{(2)}$ commonly extracted from laser-induced fluorescence (LIF) measurements:[7,18,36]

$$\mathscr{A}_0^{(2)} = \left[\frac{(2J+3)(2J-1)}{5J(J+1)}\right]^{1/2} \frac{\tilde{A}_2}{\tilde{A}_0}. \tag{12}$$

Equation (11) can then be rewritten as

$$\bar{a}_2 \propto \frac{M_{02} - M_{22}\,\mathscr{A}_0^{(2)}}{M_{00} - M_{20}\,\mathscr{A}_0^{(2)}} \left(\frac{\tilde{\beta}_2}{\tilde{\beta}_0}\right). \tag{13}$$

Analytical expressions for the M values are given in Table I (M_{02} and M_{22} are M_0 and M_2, respectively, of Ref. 27). (Note that because all M values appear in ratios, they can all be multiplied by a constant with no consequence.) For mixed branches, the M values are simply added. The E values in the table are the one-photon line strengths (often denoted S_{ij}) given by Earls.[41] All the information about the photoionization dynamics is contained in the ratio $\tilde{\beta}_2/\tilde{\beta}_0$. This ratio is a constant for all J and all branches, but is unknown. By determining the ratio of $\bar{a}_2$ values for two different branches, however, *the photoionization dynamics can be eliminated.*[25,27] Alternatively, the ratio $\tilde{\beta}_2/\tilde{\beta}_0$ can be determined from independent (1 + 1) CDAD experiments of unaligned NO.[40]

The experimentally determined ratio R of $\bar{a}_2$ coefficients for two different branches, i, and k, is given by

$$R = \frac{\bar{a}_2^{(i)}}{\bar{a}_2^{(k)}} = \frac{\left[\dfrac{M_{02}^{(i)} - M_{22}^{(i)}\,\mathscr{A}_0^{(2)}}{M_{00}^{(i)} - M_{20}^{(i)}\,\mathscr{A}_0^{(2)}}\right]}{\left[\dfrac{M_{02}^{(k)} - M_{22}^{(k)}\,\mathscr{A}_0^{(2)}}{M_{00}^{(k)} - M_{20}^{(k)}\,\mathscr{A}_0^{(2)}}\right]}. \tag{14}$$

This equation can be inverted to give $\mathscr{A}_0^{(2)}$ as a quadratic function of R. (For the range of R obtained in the present work a plot of R vs $\mathscr{A}_0^{(2)}$ for $J = 45.5$ is given later in Fig. 3.)

The advantages of the above method over the method described in Refs. 25 and 27 are twofold: first, as stated above, a wavelength spectrum to provide the relative magnitudes of the CDAD spectra is no longer necessary; second, problems arising from a difference in populations of the Λ-doubled F_1 and F_2 states are eliminated.

The analysis of PINDAD spectra, for which the ratio of a_2 to a_0 is obtained analytically from the leading two terms in the Legendre expansion [Eq. (4)], is identical to that just described for CDAD. This method was first suggested in Sec. VII of Ref. 25.

B. Magic angle PINDAD (MAP)

Theoretically, the maximum L in a PINDAD Legendre expansion [Eq. (4)] is limited only by the maximum align-

TABLE I. M expressions for (1 + 1) CDAD through the $A\,^2\Sigma$ state of NO[a].

	P	Q	R
M_{00}	$E(4\sqrt{5})$	$E(4\sqrt{5})$	$E(4\sqrt{5})$
M_{02}	$E\dfrac{2J-3}{J}$	$-E\dfrac{(2J-1)(2J+3)}{J(J+1)}$	$E\dfrac{2J+5}{J+1}$
M_{20}	$E4\sqrt{5}\dfrac{J+1}{2J-1}$	$-E(4\sqrt{5})$	$E4\sqrt{5}\dfrac{J}{2J+3}$
M_{22}	$E\dfrac{25(J+1)(2J-3)}{7J(2J-1)}$	$E\dfrac{5(11J^2+11J-15)}{7J(J+1)}$	$E\dfrac{25J(2J+5)}{7(J+1)(2J+3)}$

[a] Hund's case b. Here J is the total angular momentum of the initial state. E is the line strength as described in text.

ment in the photoionized state. (The maximum L can further be limited by a low value of J'.).[25] However, in practice, the rapid decrease in the magnitude of β_L with increasing L causes a strong suppression of the higher order a'_L. If these higher order coefficients, such as a'_4, a'_6, etc., are ignored and the PINDAD configuration is set to the magic angle of $\theta = 54.7°$, where $P_2(\cos\theta) = 0$, the intensity of the PINDAD signal becomes

$$I_{\mathrm{MAP}} = I_{\mathrm{PINDAD}}(54.7°) \approx a'_0. \tag{15}$$

Thus, a wavelength spectrum in the MAP configuration gives peaks whose heights are proportional to the excited state populations only, with no excited state alignment contribution (ignoring a'_4, a'_6, etc.).

The excited state populations can be written in terms of the ground state population and alignment using Eq. (8),

$$a'_0 = A_0\beta_0 = N(J)E\,[\tilde{A}_0C_{00} + \tilde{A}_2C_{20}]\,X_0\tilde{\beta}'_0, \tag{16}$$

where $N(J)$ is the population of the initial state and E is the one-photon line strength described earlier.[41] [$N(J)$ is unnecessary in the CDAD equations, described above, because it is eliminated in the ratio $\bar{a}_2$. The E values appear in those equations through M only because of the possibility of mixed branches.] Using Eq. (12) and expressions from Ref. 25, Eq. (15) can be expressed as

$$P\text{ branch } I_{\mathrm{MAP}} = \frac{EN\tilde{\beta}'_0}{3(2J+1)}\left[1 - \frac{J+1}{2J-1}\mathscr{A}_0^{(2)}\right], \tag{17}$$

$$Q\text{ branch } I_{\mathrm{MAP}} = \frac{EN\tilde{\beta}'_0}{3(2J+1)}\left[1 + \mathscr{A}_0^{(2)}\right], \tag{18}$$

$$R\text{ branch } I_{\mathrm{MAP}} = \frac{EN\tilde{\beta}'_0}{3(2J+1)}\left[1 - \frac{J}{2J+3}\mathscr{A}_0^{(2)}\right]. \tag{19}$$

In this case $\tilde{\beta}'_0$ is an unknown constant. It should be noted that these equations are identical to those describing polarized fluorescence from an aligned excited state.[42] From an angular momentum point of view, the fluorescence case is identical to the present one of an excited-state population produced by photoabsorption from an aligned ground state. With the ground state alignment $\mathscr{A}_0^{(2)}$ determined from the CDAD analysis, the MAP wavelength spectrum can be used to determine the ground state populations.

C. Fragment angular distributions

The angular distribution of fragment ions produced by the REMPI technique is a function of the product of probabilities for: (1) dissociation at a given angle θ (the direction of the velocity vector $\mathbf{v}$ with respect to the photolysis electric vector $\boldsymbol{\epsilon}_p$); (2) absorption of a photon by the fragment with transition dipole $\boldsymbol{\mu}_a$, where the electric vector $\boldsymbol{\epsilon}_a$ polarization is at an angle θ' from the velocity vector $\mathbf{v}$; and (3) total ionization cross section. The dynamics of the photolysis will determine the relationship between $\mathbf{v}$ and the fragment angular momentum vector $\mathbf{J}$, as well as the relation of these two vectors to the photolysis transition dipole moment $\boldsymbol{\mu}_p$, which is a function of the electronic structure of the initial and dissociative states of the parent molecule. Derivations of *correlations* between these vectors have most recently been derived for Doppler broadened spectral line profiles by Dixon[19] and Hall *et al.*[20] In this paper we have adapted the approach used by Hall *et al.*, which is somewhat more intuitively transparent, to interpret REMPI ion angular distributions.

In the experimental configuration described above, the photolysis and excitation lasers propagate in the same direction and their polarization vectors are parallel, $\boldsymbol{\epsilon}_p \| \boldsymbol{\epsilon}_a$, hence $\theta' = \theta$. We can therefore introduce a simple coordinate system which is described in detail in the Appendix. The aim is establishing this coordinate system is to obtain an expression for the ion angular distribution based on a correlation between the three vector quantities $\boldsymbol{\mu}_p$, $\mathbf{v}$, and $\mathbf{J}$. This is accomplished by fixing the angles between each of these vectors: ρ is the angle between $\mathbf{v}$ and $\boldsymbol{\mu}_p$; χ is the angle between $\mathbf{v}$ and $\mathbf{J}$; and η is the angle between $\boldsymbol{\mu}_p$ and $\mathbf{J}$. The function describing the angular distribution $I(\theta;\rho,\chi,\eta)$ is proportional to the probability of exciting the parent molecule to a dissociative state, $|\boldsymbol{\mu}_p\cdot\boldsymbol{\epsilon}_p|^2$, times the probability of exciting the daughter fragment, $\langle|\boldsymbol{\mu}_a\cdot\boldsymbol{\epsilon}_a|^2\rangle_{\mathrm{av}}$, averaged over all orientations of the parent. (The daughter excitation is averaged over all orientations of the molecule in its rotation plane, perpendicular to $\mathbf{J}$.) The angle dependence of the total ionization can be omitted as it is expected to be small.[22,38] The resultant expression for $I(\theta;\rho,\chi,\eta)$ take the form of an expansion in Legendre polynomials, i.e.,

$$I(\theta;\rho,\chi,\eta) \propto b_0[\rho,\chi,\eta] + b_2[\rho,\chi,\eta]P_2(\cos\theta) + b_4[\rho,\chi,\eta]P_4(\cos\theta), \tag{20}$$

where the b_l are different for P, Q, and R branches. Explicit expressions for the b_l are given in the Appendix [Eqs. (A12)–(A14)]. Under most experimental conditions $I(\theta;\rho,\chi,\eta)$ can only be measured to within a proportionality constant so that we define $B_l = b_l/b_0$, giving

$$I(\theta;\rho,\chi,\eta) \propto 1 + B_2[\rho,\chi,\eta]P_2(\cos\theta) + B_4[\rho,\chi,\eta]P_4(\cos\theta). \tag{21}$$

In general, experimental data are convoluted by the angular resolution of the detector. For data that are described by a Legendre expansion, the fitted coefficients $\bar{B}_l$ can be deconvoluted to coefficients for infinite angular resolution B_l using the relation[43]

$$B_l = \bar{B}_l\frac{(2l+1)(\cos\delta - 1)}{P_{l+1}(\cos\delta) - P_{l-1}(\cos\delta)}, \tag{22}$$

where δ is the angular width of the detector aperture.

IV. RESULTS AND DISCUSSION

A. General

The absorption spectrum of methyl nitrite in the 227–223 nm range covered by this work consists of a very broad featureless band (S_2) centered at 210 nm. This band has been assigned to a $\pi^* \leftarrow \pi$ transition involving an overall charge transfer from the methoxy group to the –NO moiety.[44] The diffuse nature of this band is consistent with a purely repulsive S_2 potential with the primary photoproducts being methoxy radical and NO, i.e.,

$$CH_3ONO + h\nu \rightarrow CH_3ONO^*(S_2) \rightarrow CH_3O\cdot(X) + NO(X\,^2\Pi, v, J). \tag{23}$$

The threshold energy for this dissociation is 1.8 eV,[32] so that substantial excess energy ($\sim$3.8 eV) is available for partitioning among the translational and internal degrees of freedom of the two photofragments. At wavelengths longer than 210 nm only the ground electronic states of CH_3O and NO are accessible while at shorter wavelengths CH_3O can be produced in its $\tilde{A}\,^2A_1$ electronically excited state. The repulsive nature of the S_2 state has recently been confirmed by Huber and co-workers[5] who measured the $CH_3O\cdot$ and NO translational energies and angular distributions by electron-impact photofragment spectroscopy at 248 nm. This group found that 53% $\pm$ 3% of the excess energy appears as translational energy of the fragments, in good agreement with a value of 49% expected for an impulsive dissociation mechanism involving an unbound upper state. Methyl nitrite in the S_0 state exists[45] as either the *cis* or *trans* planar (considering only the CONO) isomer; at 300 K the *cis* form is preferentially populated over the *trans* by a factor of 1.75. On the basis of the Franck–Condon principle and the repulsive nature of the S_2 potential energy surface one can readily assume that the S_2 state will retain the S_0 geometry upon excitation. Photofragment angular distributions characterize the $S_2 \leftarrow S_0$ absorption as a parallel transition with the transition dipole moment $\boldsymbol{\mu}_p$ lying in the molecular plane. The high value[5] of the photoion asymmetry parameter ($\beta = 1.4 \pm 0.1$) is also consistent with a prompt dissociation mechanism in which fragmentation is on the same time scale as parent rotation.

Additional dynamical information including internal state distributions, alignment, and other vector correlations can be derived from laser probes of the photofragments. The nascent rotational and vibrational states of NO fragment can be probed by excitation with linearly polarized light to the $A\,^2\Sigma$ state:

$$\mathrm{NO}(X\,^2\Pi, v, J) + h\nu(\sim 225\ \mathrm{nm}) \rightarrow \mathrm{NO}(A\,^2\Sigma, v', J'). \quad (24)$$

The population and alignment of the $A\,^2\Sigma$, v', J' state are probed by ionizing the NO with circularly or linearly polarized light:

$$\mathrm{NO}(A\,^2\Sigma, v', J') + h\nu(266\ \mathrm{nm}) \rightarrow \mathrm{NO}^+ + e^-. \quad (25)$$

Since the one-photon excitation process $^2\Sigma \leftarrow {}^2\Pi$ is easily characterized, populations, alignments, and vector correlations can be obtained for the $X\,^2\Pi$, v, J state of the NO fragment from the photoelectron and photoion signals.

For NO in its $X\,^2\Pi$ state one cannot speak of one ground state but rather of four. The two spin states F_1 ($^2\Pi_{1/2}$) and F_2 ($^2\Pi_{3/2}$) arise from two possible spin–orbit couplings of the total nonspin angular momentum **K** and the spin angular momentum **S**, yielding the total angular momentum $\mathbf{J} = \mathbf{K} + \mathbf{S}$, in which $J = K + 1/2$ for F_1 and $J = K - 1/2$ for F_2.[46] Each of these spin states is further split by weak coupling (Λ doublet) of the electronic angular momentum **L** with the rotation of the nuclei. This coupling is weak in Hund's cases (a) and (b),[46] however each of the Λ states ($\Lambda = \pm 1$ for a Π state) have different parities. In the case of NO, the Λ doublets arise from two orientations of the *unpaired* $p\pi$ electron lobe which lies perpendicular to the molecular axis of the NO and is either (1) parallel to **J** or (2) perpendicular to **J**. The symbols $\Pi_{A'}$ and $\Pi_{A''}$ designate cases (1) and (2), respectively.[48] The $\Pi_{A'}$ states are probed with the $Q_{11} + P_{21}$ and $Q_{22} + R_{12}$ branches (and also R_{21} and P_{12}); and $\Pi_{A''}$ states are probed with the P_{11} and $P_{22} + Q_{12}$ branches (and also $R_{11} + Q_{21}$, and R_{22}).

B. Magic angle PINDAD spectrum

The magic angle PINDAD (MAP) configuration provides a relatively simple means for obtaining ground state rotational populations, as is evident from Eqs. (17)–(19). Figure 1 shows a MAP spectrum of NO produced from the dissociation of methyl nitrite. Two distinct features are apparent: (1) at longer wavelengths the bandhead region shows NO at relatively low J; (2) at shorter wavelengths very high-J photofragments are observed. The low-J region is attributed to free NO contaminant in the sample. Indications that this region is indeed due to free NO and not an alternate dissociation path come from the photoion time-of-flight spectra; the long wavelength region shows a very sharp and narrow peak corresponding to a low velocity NO; while the short wavelength region shows two distinct peaks (see end of Sec. II) corresponding to NO with an average energy of $\approx$1 eV. It is extremely improbable that NO with low J is a product of photodissociation; very low translational and low rotational energy products are inconsistent with high excess energy ($\sim$3.8 eV) above dissociation, particularly for the nonlinear RO–NO geometry. (If this were the case then all of the photolysis energy would be channeled into internal degrees of freedom of the $\cdot OCH_3$ radical; conservation of angular momentum would then dictate that these be vibrational modes.)

The lower panel of Fig. 1 shows the high J region in detail with assignments for four of the strongest NO branches: P_{11}, $Q_{11} + P_{21}$, $Q_{22} + R_{12}$, and $P_{22} + Q_{12}$. (The $R_{11} + Q_{21}$ and R_{22} branches are expected to peak at similar J, which would place the strong lines of these branches at shorter wavelengths and outside the range of the figure.) The R_{21} and P_{12} branch lines are present in our spectrum, but as they are weak we do not report their assignment. The assignment is based on molecular constants for the $X\,^2\Pi$ and $A\,^2\Sigma$ states listed in Huber and Herzberg[47] and expressions for the energies of these states given in Herzberg.[46] Relative populations of the $X\,^2\Pi$, $v = 0$ rotational states can be extracted from the spectral line intensities (peak heights, see Sec. II) by using Eqs. (17)–(19). The branch and J dependent line strengths E are easily calculated.[41] The only unknown in these equations is the alignment $\mathscr{A}_0^{(2)}$, which is obtained from the CDAD measurements (the other unknown, $\bar{\beta}_0'$, is unimportant for relative population measurements). Once the alignment is known then populations $N(J)$ can be reported for each of the branches. An examination of Fig. 1 reveals that the MAP signal for the Q branches is much lower than for P branches. In the case that $\mathscr{A}_0^{(2)} = 0$ and $N(J)$ are equal for all initial Λ-doublet states, the line strengths E dictate that I_{MAP} should be higher for a $Q_{11} + P_{21}$ branch (probing $F_1\,\Pi_{A'}$) than for a P_{11} branch (probing $F_2\,\Pi_{A''}$) by a factor of $\approx$2. (The P_{21} component makes a small contribution to the $Q_{11} + P_{21}$ branch, being about a factor of 10 lower than the Q_{11} component.) As is

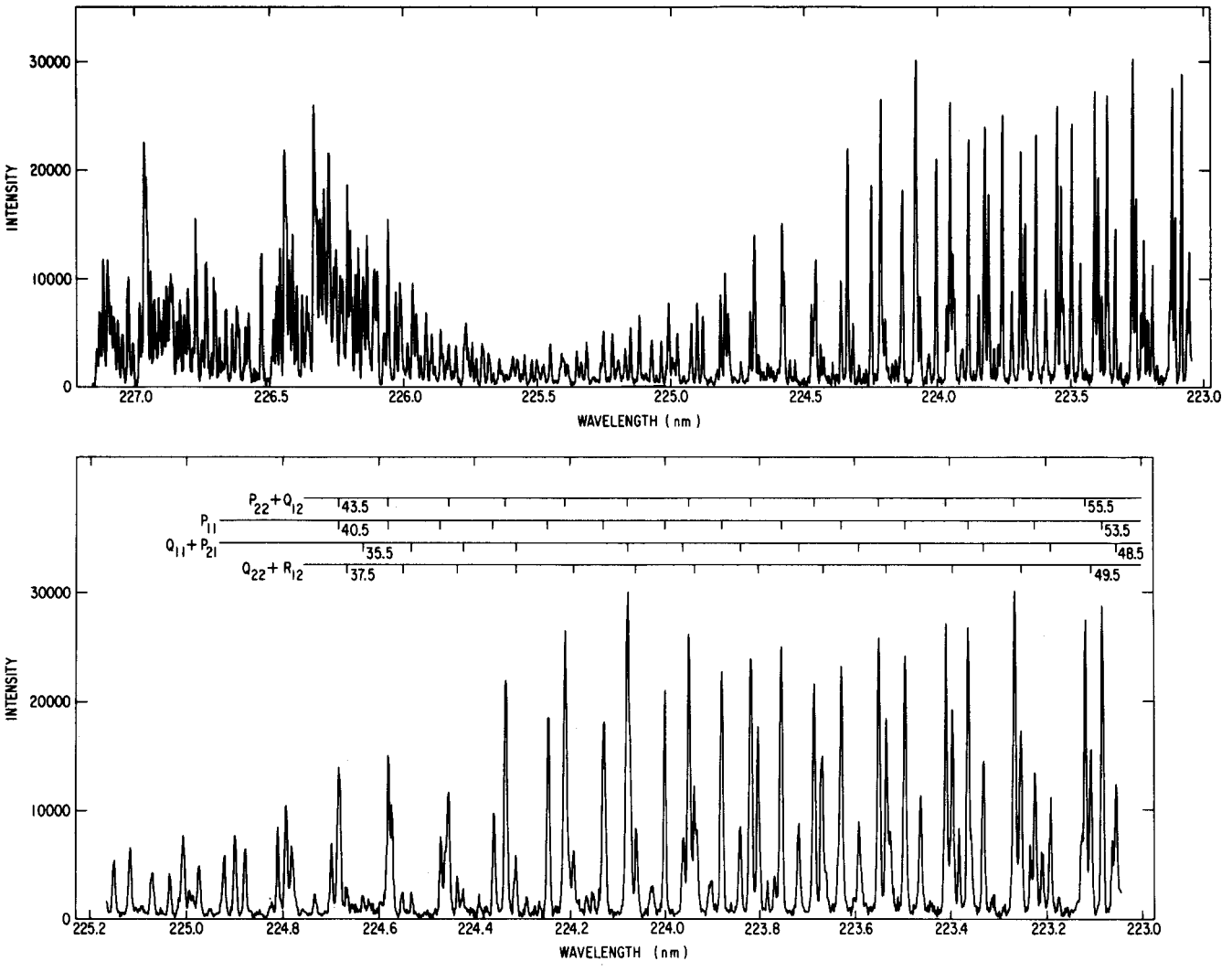

FIG. 1. Magic angle PINDAD spectrum of NO ($v = 0$) from the photodissociation of CH_3ONO. The left (longer wavelength) region corresponds to free NO. The lower panel is an expansion of the region corresponding to high J.

shown in the next section, the decrease in the Q branch intensity can be attributed to a negative $\mathscr{A}_0^{(2)}$ and/or to a lower population for initial Λ-doublet states probed by that branch.

C. Alignment from CDAD

Representative CDAD spectra are shown in Fig. 2 and are summarized in Table II in terms of the $\bar{a}_2$ coefficients of Eq. (6). The most striking feature of the photolysis CDAD spectra is the apparent lack of CDAD signal for the Q branches ($\bar{a}_2 \sim 0$). This result is in contrast to the CDAD spectrum for free, unaligned NO (dashed line, $\bar{a}_2 \sim +0.069$). On the other hand, photolysis CDAD spectra for the P branches are enhanced relative for unaligned NO. (The free NO spectra are from a previous study[29] for different J, but are expected [38] to resemble closely those branches of interest here at $J = 45.5$.) As discussed below, these observations are a direct signature of a high negative value for $\mathscr{A}_0^{(2)}$. The experimentally derived ratio $R = \bar{a}_2^{(Q_{11}+P_{21})}/\bar{a}_2^{(P_{11})}$ [Eq. (14)] for a range of J's in Table II results in a value of $\mathscr{A}_0^{(2)} = -0.45 \pm 0.04$ averaged over J and both the F_1 and F_2 states. The relationship between R and $\mathscr{A}_0^{(2)}$ at $J = 45.5$ is shown graphically in Fig. 3. Because the values of $\bar{a}_2^{(Q_{11}+P_{21})}$ are very small, and therefore difficult to determine accurately, the R values have a corresponding uncertainty associated with them. However, as is evident from Fig. 3, the value of $\mathscr{A}_0^{(2)}$ is fairly insensitive to small changes in R about $R = 0$.

For an initial state with an alignment characterized by $\mathscr{A}_0^{(2)} \sim -0.4$, low $|M_J|$ substates have a greater population relative to high $|M_J|$ states. Upon photoabsorption, the effect of a Q transition is to "wash out" this M_J anisotropy in the excited state. Specifically, the initial state alignment, with low $|M_J|$ preferentially populated, is reduced in the excited state by the relative Q branch transition probabilities which preferentially excite high $|M_J|$ levels ("parallel" transition, $\mathbf{J} \| \boldsymbol{\mu}_a$). This trend is confirmed quantitatively by comparing the A_2/A_0 ratio for an excited state populated via a Q branch transition from an unaligned initial state ($\mathscr{A}_0^{(2)} = 0.0$), $A_2/A_0 = +0.89$, to that for an aligned initial state with $\mathscr{A}_0^{(2)} = -0.4$, $A_2/A_0 = +0.32$. This drop in A_2/A_0 is accompanied by an increase in the hexadecapole moment, A_4/A_0, which changes from 0.0 to -0.57 for initial state alignment of $\mathscr{A}_0^{(2)} = 0.0$ and $\mathscr{A}_0^{(2)} = -0.4$, respectively.

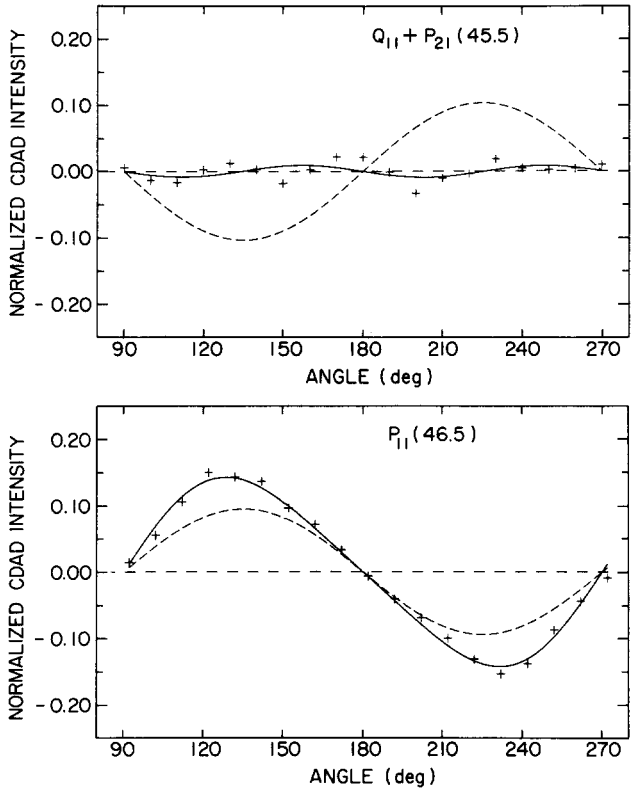

FIG. 2. CDAD angular distributions of NO ($v = 0$) from the photodissociation of CH_3ONO. The + are experimental data. The solid curves are best fits to the data using Eq. (2), with $L = 2$ and 4. The dashed curves are for free (unaligned, $\mathscr{A}_0^{(2)} = 0.0$) NO (see note in Sec. IV C of the text).

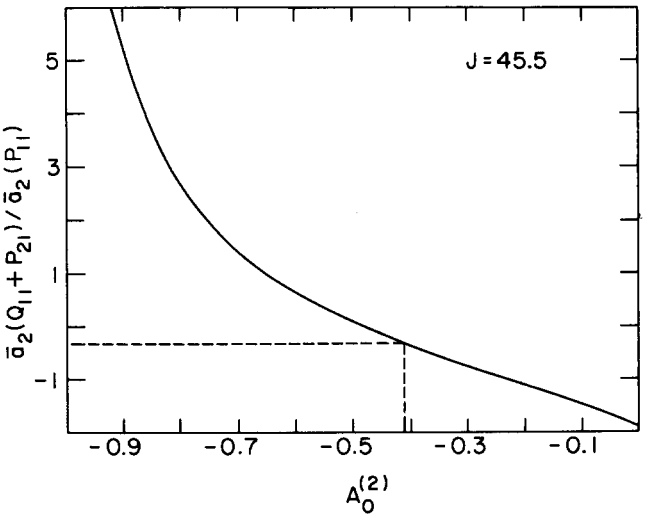

FIG. 3. A plot of the CDAD ratio, Eq. (14), for $Q_{11}+P_{21}$ and P_{11} branches with $J = 45.5$, in the region of negative alignment. The dashed line indicates the theoretical limit for the alignment parameter $\mathscr{A}_0^{(2)} \geqslant -0.413$ [see Eq. (27)]; the corresponding CDAD ratio is -0.307.

The hexadecapole contribution is not reflected in the CDAD spectrum due to the small value of $\bar{\beta}_4$ relative to $\bar{\beta}_2$. This, however, is not a significant loss of information about the M_J populations in the initial ground state, since for a one-photon dissociation the alignment is characterized by quadrupole moments only (for a fragment-velocity-averaged ensemble).

For a P or R branch transition where low M_J substates are preferentially excited ("perpendicular transition" $\mathbf{J}\perp\boldsymbol{\mu}_a$), the initial state alignment of $\mathscr{A}_0^{(2)} \sim -0.4$ *enhances* the excited state alignment relative to the case for excitation from an unaligned state. This increase is reflected in the P_{11} (45.5) CDAD spectra of Fig. 2. The enhancement of alignment in the P branch further contributes of the lack of Q branch CDAD intensity (Fig. 2), because the mixed branch $Q_{11}+P_{21}$ has both a depressed Q alignment and an enhanced P alignment which tend to cancel. The strong negative alignment of the NO photofragment is consistent with the MAP spectrum (Fig. 1) which shows a strong enhancement of P branch lines relative to Q branch lines as is predicted by Eqs. (17)–(19).

TABLE II. CDAD fitting and alignment parameters.

Branch	J[a]	$\bar{a}_2$[b]	$\mathscr{A}_0^{(2)}$[c]
P_{11}	35.5–36.5	− 0.085	− 0.45 ± 0.05
$Q_{11}+P_{21}$		0.017	
P_{11}	44.5–46.5	− 0.084	− 0.44 ± 0.03
$Q_{11}+P_{21}$		0.015	
$P_{22}+Q_{12}$	45.5–46.5	− 0.074	− 0.46 ± 0.04
$Q_{22}+R_{12}$		0.008	

[a] Reported values are averaged over several runs and J's.

[b] The CDAD data were fitted to $\bar{a}_2$ and $\bar{a}_4$ as in Eq. (2). [The $\bar{a}_2$, as well as $\bar{a}_4$, are related to the a_2 and a_4 by Eq. (6). However, only the $\bar{a}_2$ are needed to obtain $\mathscr{A}_0^{(2)}$.]

[c] The alignment parameter $\mathscr{A}_0^{(2)}$ is obtained from the $\bar{a}_2$'s of two distinct branches as described in Sec. III A. The average value, weighted by number of runs, is $\mathscr{A}_0^{(2)} = -0.45 \pm 0.04$.

The experimental result $\mathscr{A}_0^{(2)} = -0.45 \pm 0.04$ should be compared to its theoretical limit. For fragment alignment created by one-photon dissociation, only the $L = 0$ and 2 terms of Eq. (1) are applicable, and this equation can be written explicitly as

$$N_{M_J} = \frac{1}{2J+1}\left[1 + \frac{5[3M_J^2 - J(J+1)]}{(2J+3)(2J-1)}\,\mathscr{A}_0^{(2)}\right]. \tag{26}$$

This equation gives the relative initial M_J substate populations for a given initial state alignment. The fact that the value of N_{M_J} represents a population, and therefore cannot be less than zero, imposes the following constraint on $\mathscr{A}_0^{(2)}$:

$$\mathscr{A}_0^{(2)} \geqslant \frac{-(2J+3)}{5J}, \tag{27}$$

where this lower limit is obtained by requiring that $N_{(M_J=\pm J)}$ be nonnegative. For $J = 35.5$ Eq. (27) provides the limit $\mathscr{A}_0^{(2)} \geqslant 0.417$ while for $J = 45.5$, $\mathscr{A}_0^{(2)} \geqslant -0.413$. The experimental result of $\mathscr{A}_0^{(2)} = -0.45 \pm 0.04$ is consistent with these limits within the given experimental error. Note that for high J, Eq. (27) approaches the well known classical limit[18] of $\mathscr{A}_0^{(2)} \geqslant -0.4$.

While the J-averaged experimental $\mathscr{A}_0^{(2)}$ is consistent with theoretical limits discussed above, the results appear to be systematically lower (more negative) than these limits.

Two factors can be suggested to account for this result: (1) saturation in the excitation of the NO fragment could distort the M_J distribution in the A state; (2) incomplete overlap of the laser linewidth with the Doppler-broadened NO absorption line could result in preferential sampling of certain fragment velocities. Although we measured CDAD signals at a range of laser energy densities, and found no detectable change in the fitted $\bar{a}_2$ parameters, we cannot completely rule out small saturation effects because the dynamic range of this experiment is too small to perform a complete power dependence study. Jacobs, Madix, and Zare[22] have demonstrated that a one-color 1 + 1 REMPI spectrum of NO cannot be completely free of saturation; at energy densities below 0.5 mJ/cm^2 saturation does not appear to be a significant complication, while at 5 mJ/cm^2 it may be a problem. Under the operating conditions outlined in the experimental section an energy density near 5 mJ/cm^2 is achieved. This may present a difficulty for the branches with low CDAD signal, $Q_{11}+P_{21}$ and $Q_{22}+R_{12}$, where even a small degree of saturation could reduce the already small $\bar{a}_2^{(Q)}$. The second problem was found to be significant in laser fluorescence studies of photodissociation products, where alignment was strongly influenced by the laser linewidth.[50] In our experiments the laser linewidth is ~ 1.3 cm^{-1} (full width at half-maximum), which is broader than the Doppler width of 0.74 cm^{-1} (full width at base line) for 1 eV NO fragments. Although the Gaussian laser line completely envelopes the Doppler profile (which has a rather sharp rise and fall at the base line), to some extent it preferentially samples the center of the profile where laser intensity is greatest. The Doppler profile center corresponds to fragment velocities ($\mathbf{v}$) which are parallel to the laser polarization ($\boldsymbol{\epsilon}_p$) as a result of the highly peaked photofragment angular distribution[5] along $\boldsymbol{\epsilon}_p$. Since $\mathbf{J}$ is essentially perpendicular to $\mathbf{v}$ (see Sec. IV E), fragments at the Doppler profile center will also have $\mathbf{J}$ perpendicular to $\boldsymbol{\epsilon}_p$ which corresponds to M_J distributions peaked near $|M_J| \sim 0$. Preferential excitation of these fragments would result in an apparently more negative $\mathscr{A}_0^{(2)}$.

In light of the above discussion, we conclude that the NO fragments from photodissociated methyl nitrite are at the maximum (most negative $\mathscr{A}_0^{(2)}$) alignment for both the F_1 and F_2 initial states. This result indicates that low M_J substates are preferentially populated in the photoproducts, such that the angular momentum vector $\mathbf{J}$ is perpendicular to the electric vector $\boldsymbol{\epsilon}_p$ (the axis of quantization), and therefore to the photolysis transition dipole moment of the parent $\boldsymbol{\mu}_p$ during photofragmentation ($\eta = 90°$).

D. Rotational state populations

The state distributions $N(J)$ for the $F_1\Pi_{A'}$, $F_1\ \Pi_{A''}$, $F_2\Pi_{A'}$, and $F_2\Pi_{A''}$ levels of the X state of NO are obtained from the alignment corrected MAP intensities for the P_{11}, $Q_{11}+P_{21}$, $P_{22}+Q_{12}$ and $Q_{22}+R_{12}$ branches, respectively, and are shown in Fig. 4. The overall population distribution is well characterized by a Gaussian distribution (also shown in Fig. 4) with a peak value of $J_p = 51 \pm 2$ and width at half-maximum of $J_{\mathrm{FWHM}} = 12 \pm 2$. These fitted parameters can only be viewed as representative since the experimental data are limited to rotational levels with $J \leqslant 55.5$. Gaussian-like

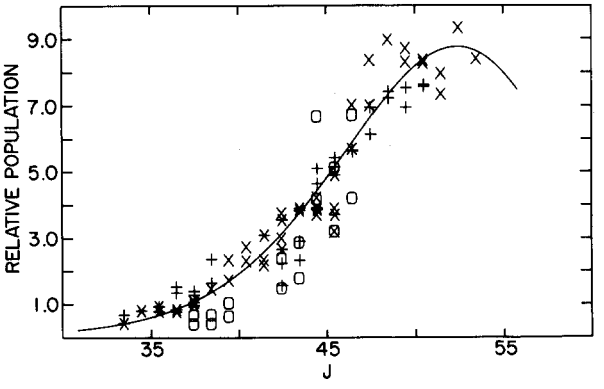

FIG. 4. Rotational state distributions for NO ($v = 0$) photodissociated from CH_3ONO. The curve is a best fit to a Gaussian [in $J(J+1)$], with $J_p = 51 \pm 2$ and $J_{\mathrm{FWHM}} = 12 \pm 2$. The symbols are $\times$ for $F_2\Pi_{A'}$ (probed by $P_{22}+Q_{12}$), + for $F_1\Pi_{A'}$ (probed by P_{11}), * for $F_2\Pi_{A''}$ (probed by $Q_{22}+R_{12}$), and O for $F_1\Pi_{A''}$ (probed by $Q_{11}+P_{21}$). The heights of the distributions for each of the spin–orbit, Λ-doublet states are normalized to a single arbitrary value.

rotational state distribution have also been found for NO photofragments produced via the S_1 state of CH_3ONO[6,10,12] and other precursor molecules such as $(CH_3)_2N$–NO,[7] ClNO,[49] and $(CH_3)_3CONO$.[17] Quantal and classical trajectory calculations by Schinke[51,52] have shown that inverted (highly non-Boltzmann) rotational distributions are a natural consequence of rotational–translational coupling in the direct dissociation of pseudotriatomic molecules. Furthermore, Schinke found that rotational distributions are governed by the "rotational reflection principle" in which the distribution of rotational angular momentum of the diatomic fragment reflects the distribution of initial orientation angles (representative of the nonlinearity) of the parent molecule. According to the rotational reflection principle, the high degree of population inversion observed in Fig. 4 results from a highly anisotropic S_2 potential energy surface above the bent ground state (S_0) equilibrium geometry. Calculations of this type could provide additional information on the extent of the rotational–translational coupling in the repulsive S_2 state and the distributions of O–N–O bending and torsion angles in the initial S_0 state.

Assuming that the Gaussian fit in Fig. 4 correctly describes the NO (X, $v = 0$) rotational distribution, we obtain an average rotational energy of $\langle E_{\mathrm{rot}} \rangle = 4600 \pm 200$ cm^{-1}. This value brackets the result obtained from impulsive model calculations ($\langle E_{\mathrm{rot}} \rangle = 4600$ cm^{-1}) of Keller *et al.*[4,5] using $\cdot OCH_3$ and NO photofragment translational energies measured at 248 nm (S_2 dissociation). In the impulsive model, rotational excitation results from the torque exerted on the molecular fragment by the motions of the recoiling atoms along the dissociation coordinate. Scaling the impulse model calculations for the increase in total available energy, we estimate $\langle E_{\mathrm{rot}} \rangle = 5340$ cm^{-1} at a dissociation wavelength of 225 nm which corresponds to the center wavelength of the MAP spectrum (Fig. 1). Given the approximation nature of such calculations and the limitations of the fit in Fig. 4, the agreement with experiment is quite satisfactory and suggests that the mechanism for producing rotationally

excited NO via S_2 dissociation is well described by the impulsive model.

The relative preference for dissociation into the four electronic state channels ($F_1\Pi_{A'}$, $F_1\Pi_{A''}$, $F_2\Pi_{A'}$, $F_2\Pi_{A''}$) of NO ($X\,^2\Pi$) was obtained by averaging the rotational population data (over J) in Fig. 4 for the appropriate rotational excitation branches. The results can be summarized as follows:

$$\frac{N(\Pi_{A'})}{N(\Pi_{A''})} = 1.4 \pm 0.1(F_1),$$

$$\frac{N(\Pi_{A'})}{N(\Pi_{A''})} = 0.9 \pm 0.1(F_2),$$

$$\frac{N(F_1)}{N(F_2)} = 1.3 \pm 0.1(\Pi_{A'}),$$

$$\frac{N(F_1)}{N(F_2)} = 0.85 \pm 0.1(\Pi_{A''}).$$

The F_1 ($\Pi_{1/2}$) $\Pi_{A'}$ channel is favored above all others and the F_1 ($\Pi_{1/2}$) spin–orbit state shows preferential alignment of the lone $p\pi$ orbital in the plane of rotation [$N(\Pi_{A'}) > N(\Pi_{A''})$]. This "electronic alignment" of the F_1 levels can be rationalized given the $S_2 \leftarrow S_0$ dissociation dynamics as inferred so far. Specifically, the S_2 state is known to be of A' symmetry (C_s symmetry group) which requires the S_2 electronic wave function to be symmetric with respect to reflection in the C–O–N–O molecular plane. Consequently, the $p\pi$ orbitals of the NO group which contribute to the π^* molecular orbital (a') must also lie in that plane. Since photodissociation via the S_2 state results in NO fragments preferentially rotating in the molecular plane ($\mathscr{A}_0^{(2)} \approx -0.4$), an enhanced population in the $\Pi_{A'}$ component of the $p\pi$ orbital is expected. Similar qualitative arguments have been used to rationalize the Λ-doublet populations resulting from the $S_1 \leftarrow S_0$ dissociation of other alkyl nitrites.[3,6,11,16,17] For the $F_2(^2\Pi_{3/2})$ state the Λ-doublets are populated nearly equally. By contrast, Schwartz-Lavi and Rosenwachs[17] obtained quite different $N(\Pi_{A'})/N(\Pi_{A''})$ ratios in a very recent study of the S_2 dissociation of the closely related system, *t*-butyl nitrite. They find that the $\Pi_{A''}$ levels are strongly preferred for $49.5 \leqslant J \leqslant 60.5$ with an average $N(\Pi_{A'})/N(\Pi_{A''})$ of 1/2.7. In order for the parent S_2 state to be of overall A' symmetry, they rationalized that the unobserved $\cdot OC(CH_3)_3$ fragment must also have A'' symmetry. Although S_2 photodissociation for both parent molecules leads to NO photofragments with similar rotational alignments and rotational state distributions ($\mathscr{A}_0^{(2)} = -0.30 \pm 0.06$, $J_p \approx 53.5$ for *t*-butyl nitrite), the disparity in the Λ-doublet populations reflects subtle differences in their respective dissociation mechanisms.

The results for the rotationally averaged $N(F_1)/N(F_2)$ ratios given above show a spin–orbit preference for the $\Pi_{A'}$ levels whereas an approximately statistical ratio is found for the $\Pi_{A''}$ components. The data of Schwartz-Lavi and Rosenwachs[17] for *t*-butyl nitrite also show a small preference for the F_1 state of NO following $S_2 \leftarrow S_0$ photodissociation. In general, spin alignment is not expected in the direct dissociation of repulsive singlet states unless curve crossing occurs to higher spin states in specific exit channels.[53] Specific mechanisms have been invoked to account for such spin alignment in $CN(X\,^2\Sigma^+)$ and OH ($X\,^2\Pi$) from photodissociation of ICN[54] and HONO,[3] respectively, however, such mechanisms are not readily generalized to the present study. In any case, the F_1 and F_2 states represent distinct dissociation channels and their relative yields should be a sensitive probe of additional energy and angular momentum transfers not considered in simple impulsive dissociation models.

E. Photoion angular distributions

Figure 5 shows the time-of-flight distribution of NO photoions at a representative range of wavelengths, at $\theta = 0°$. Given the geometry of the drift and accelerating regions, the TOF difference between the fast (forward) and slow (backward) NO^+ photoions at 0° can be used to obtain an estimate of the NO fragment translational energy imparted by dissociation. A translational energy of ≈ 1 eV is obtained from this analysis which is very close to that measured[4,5] for NO fragments produced at 248 nm when scaled to reflect the increase in excess energy at 223.5 nm ($\langle E_{tr} \rangle_{225} \approx 1.17\ \langle E_{tr} \rangle_{248} = 8140\ cm^{-1} = 1.01$ eV). In principle, it is also possible to use photoion TOF data such as that shownin Fig. 5 to extract the translational energy distribution for each J and thereby provide a more detailed energy partitioning of the dissociation process, particularly for the unobserved $\cdot OCH_3$ fragment. Although desirable, such an investigation in beyond the scope of the present work.

Photoion angular distributions for the P_{11} and $Q_{11} + P_{21}$ branches with $J = 46.5$ are presented in Fig. 6. A fit of the experimental data to fourth order Legendre polynomials [Eq. (20)] is shown as the solid line. Since the velocity of the fragment NO is so much greater than that for the parent CH_3ONO, the lab to center-of-mass transformation angle $\tilde{\Theta}$ is small ($\theta_{cm} = \theta_{lab} - \tilde{\Theta}$, where $\tilde{\Theta} \equiv \sin^{-1}(v_{cm}/v_{NO})$, v_{cm} is the velocity of the center-of-mass system in the lab frame, and v_{NO} is the velocity of the NO fragment in the center-of-mass frame),[55] and therefore the lab and center-of-mass angles are virtually the same. The fitting coefficients $\overline{B}_2$ and $\overline{B}_4$ are corrected (deconvoluted) for the detector collection angle using Eq. (22) and then used to extract the angles ρ, χ, and η. The results for the four substates of NO at $J = 46.5$ are summarized in Table III. Since the CDAD results indicate a maximum alignment with

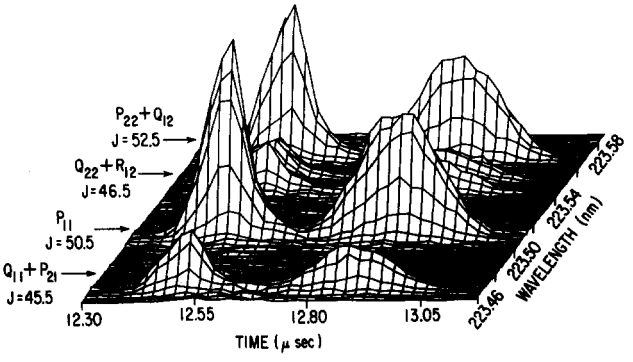

FIG. 5. REMPI photoion time-of-flight spectrum of NO($v = 0$) photoproduct as a function of wavelength. The polarization of the dissociation–excitation laser is along the detector axis ($\theta = 0$).

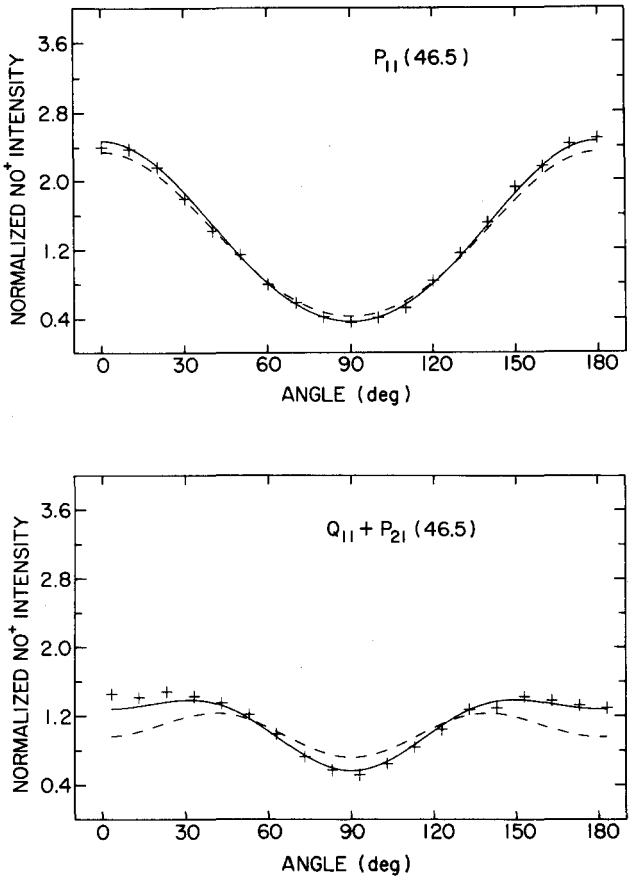

FIG. 6. Normalized REMPI photoion angular distributions of photofragment NO ($v = 0$) at $J = 45.5$ for two branches. The + are experimental data. The solid curves are best fits to the data with Eq. (21). The dashed curves are for the case of $\rho = 27°$, $\chi = 90°$, and $\eta = 90°$. The parameters characterizing the solid curves are given in Table III.

$\mathbf{J} \perp \boldsymbol{\mu}_p$, we constrain η to be $\approx 90°$; the other two angles, χ and ρ, are fitted to the data manually by varying the angles such that best agreement is attained between the calculated and experimentally extracted B_2 and B_4 coefficients. (Figure 7 provides a useful visual representation of the three vectors and the angles between them, on the molecular frame of the methyl nitrite molecule in the process of dissociation.) It should be noted that the B_2 and B_4 coefficients are strongly branch dependent (see Appendix); consequently, very similar angular correlations (ρ, χ, η) can result in quite different B_l.

The dashed curves in Fig. 6 are for the case of $\rho = 27°$, $\eta = 90°$, and $\chi = 90°$. The value of $\rho = 27°$ was obtained by Keller *et al.*[4,5] from a study of the total (unresolved internal states) angular distribution for S_2 photolysis at 248 nm. This set of correlation angles corresponds to a dissociation mechanism which is constrained to a plane containing the –O–N–O group and $\boldsymbol{\mu}_p$. The fact that these angles reproduce the basic features of the experimental photoion angular distributions (Fig. 6) attests to the overall correctness of a planar dissociation process.

The gross features of the curves in Fig. 6 can be anticipated from the CDAD alignment result, $\eta = 90°$, which indicates that $\mathbf{J} \perp \boldsymbol{\epsilon}_p$, and from the essentially planar geometry of the dissociation complex. For a fast dissociation of planar excited CH_3ONO^* it is expected that J be approximately perpendicular to v. If we assume that ρ ($\mathbf{v} \angle \boldsymbol{\epsilon}_p$) is small, the majority of the NO fragments appear along the direction of the electric vector $\boldsymbol{\epsilon}_p$, with J perpendicular to $\boldsymbol{\epsilon}_p$ ($\boldsymbol{\epsilon}_p \| \boldsymbol{\epsilon}_a$). Since P and R branches are perpendicular transitions they will be preferentially excited at $\theta = 0°$ (and 180°) since $\mathbf{J} \perp \boldsymbol{\epsilon}_a$. Since the NO flux peaks at these angles high REMPI ion signals can be accounted for. In contrast, Q branches, which are parallel transitions, should be preferentially excited when $\theta = 90°$ (J is now parallel to $\boldsymbol{\epsilon}_a$), however the fragment flux is a minimum at this angle. Therefore Q branch transitions will have minima at $\theta = 0°$ and 180° due to low Q branch excitation probability, and at $\theta = 90°$ due to low NO flux. These expectations are qualitatively borne out in the results shown in Fig. 6 and the $F_1\Pi_{A'}$, $F_1\Pi_{A''}$ and $F_2\Pi_{A'}$ results listed in Table III, but not for the $F_2\Pi_{A''}$ state. The J–v correlation for the $F_2\Pi_{A''}$ state indicates a significant deviation from planarity, $\chi = 62°$, in the dissociation complex. At this value of χ the $F_2\Pi_{A''}$ angular distribution curve resembles that for $F_1\Pi_{A'}$ rather than the $F_1\Pi_{A''}$. The sensitivity of the $F_2\Pi_{A''}$ to χ is quite dramatic in the range $65° \leqslant \chi \leqslant 75°$, where the B_4 coefficient changes from -0.78 ($\chi = 75°$) to $+0.20$ ($\chi = 65°$) with $\rho = 20°$ and $\eta = 85°$ ($B_2 = 0.86$ for $\chi = 75°$, while $B_2 = 1.17$ for $\chi = 65°$). The sensitivity of the B_2 and B_4 coefficients varies with each angle, χ, ρ and η, and their range of values; in general, a 5° change in one of the angles results in a 5%–10% change in the coefficients.

The vector correlations summarized in Table III are very distinct for each of the spin–orbit, Λ–doubled state. According to the rotational reflection principle,[51,52] a specific geometry of the ground state parent molecule results in a specific vibrational–rotational state as well as a specific geometrical relation of the fragments with respect to the parent molecular frame. A broader interpretation of the rotation reflection principle may imply that each of the four states, $F_1\Pi_{A'}$, $F_1\Pi_{A''}$, $F_2\Pi_{A'}$ and $F_2\Pi_{A''}$ originate from different geometries of ground state methyl nitrite. Since the equilibrium (most probable) geometry of the CH_3ONO is planar, the predominant fragment orientations should reflect this geometry. Photofragmentation from a strictly planar geometry of the CH_3ONO will result in $\chi = 90°$. To some extent this is the case, because for the $F_1\Pi_{A'}$ state, which is the most fa-

TABLE III. NO photoion angular distribution parameters and photodissociation vector correlations.[a]

State[b]	B_2[c]	B_4[c]	ρ $\mathbf{v} \angle \boldsymbol{\mu}_p$	χ $\mathbf{v} \angle \mathbf{J}$	η $\mathbf{J} \angle \boldsymbol{\mu}_p$
$F_1\Pi_{A'}$	1.78	0.30	24(2)°	83(2)°	90(2)°
$F_1\Pi_{A''}$	0.86	−0.95	13(2)°	79(2)°	90(2)°
$F_2\Pi_{A'}$	1.75	0.04	20(2)°	70(3)°	87(3)°
$F_2\Pi_{A''}$	1.30	0.44	22(2)°	62(3)°	83(3)°

[a] NO, $v = 0$, $J = 46.5$.
[b] The $F_1\Pi_{A'}$ state is probed by P_{11} branch, the $F_1\Pi_{A''}$ by the $Q_{11} + P_{21}$, the $F_2\Pi_{A'}$ by the $P_{22} + Q_{12}$, and the $F_2\Pi_{A''}$ by the $Q_{22} + R_{12}$.
[c] The B_2 and B_4 parameters are from Eq. 21, and have been deconvoluted from the experimental data using Eq. (22).

vored dissociation channel, χ is closer to 90° than for the $F_2\Pi_{A'}$ state. Since nonplanar geometries are less probable, one could account for the lower yield of NO in the $F_2\Pi_{A'}$ state. In addition, smaller χ angles could result from a "twist" induced by the S_2 potential energy surface in specific channels. Clearly, in order to distinguish the effects of partent geometry and features of the potential energy surface a calculation of the S_2 surface is necessary as well as an evaluation of the dynamics on that surface.

The values of ρ extracted from the fits of the data in Table III are not necessarily inconsistent with that obtained by Keller *et al.*[4,5] ($\rho = 27°$), since their results correspond to ρ averaged over all states of the NO fragment. For the F_1 ($^2\Pi_{1/2}$) levels, the $\Pi_{A'}$ and $\Pi_{A''}$ components exhibit very different ρ angles ($\mu_p \angle \mathbf{v}$) which would appear to be correlated to the distinct orientations of the NO one-electron $p\pi$ orbital relative to the dissociation plane. The distinction is reduced for the F_2 ($^2\Pi_{3/2}$) final states for which nonplanar conformations of CH_3ONO (implied by $\chi \leqslant 70°$) are seemingly more important.

The photoion angular distributions for the F_2 states are best fitted with $\eta = 87°$ ($\Pi_{A'}$) and 83° ($\Pi_{A''}$), which deviate from the CDAD result of a maximum alignment, $\eta = 90°$. These are not significant deviations in light of the error range in the CDAD and photoion data. It should be pointed out that this method of analysis of REMPI photoion angular distributions does not include weighted distributions of angles ρ, χ, and η; each angle is assumed to have a fixed value. Therefore, these reported angles represent most probable values rather than rigid quantities. Nonetheless, our data provide an example of a method for quantitatively obtaining angular correlations in terms of angles between relevant dynamical vectors. These correlations can be employed to infer detailed characteristics of the dissociation mechanism, such as the geometry of the parent molecule and the shape of the dissociative surface.

V. SUMMARY

A combination of angle-resolved photoelectron and photoion REMPI techniques have been used to probe NO($X\,^2\Pi$, $v = 0$) photofragments produced by dissociation of CH_3ONO via the S_2 state. Photoelectron measurements in the CDAD and PINDAD configurations yielded initial state alignments ($\mathbf{J} \angle \mu_p$) for the first time and provided rotational and electronic state distributions. A semiclassical analysis scheme has been presented for extracting vector correlations between μ_p, $\mathbf{v}$, and $\mathbf{J}$ from photoion angular distributions.

The qualitative features of the S_2 dissociation process as derived from earlier investigations[4,5,32,44] and from this work are shown pictorially in Fig. 7. Photoexcitation to the repulsive S_2 state results in dissociation in which electronic energy is channeled into an "impulse" along the RO–NO bond resulting in a rotation and translation of the fragments as the bent parent molecule breaks up. Recoil of the fragments along the dissociation coordinate creates a torque which is responsible for the NO fragment rotation with $\mathbf{J}$ nearly perpendicular to the molecular plane of the parent. The high translational ($\langle E_{tr} \rangle \approx 8100\ cm^{-1}$) and high rotational

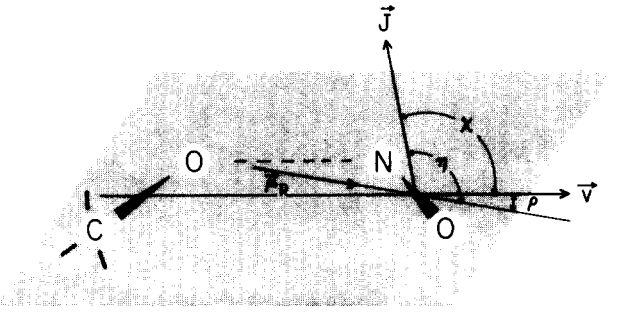

FIG. 7. Diagram of photodissociating methyl nitrite. The S_2 (A') ← S_0(A') transition dipole moment μ_p, the velocity $\mathbf{v}$, and the angular momentum $\mathbf{J}$ of the NO fragment are superimposed over the molecular frame, along with the appropriate angles between these vectors.

($\langle J \rangle = 51$ and $\langle E_{rot} \rangle \approx 4600\ cm^{-1}$) energies of the NO photofragment imply a very fast dissociation with minimal randomization of internal degrees of freedom in the photoexcited CH_3ONO. These energies are in substantial agreement with that expected from impulsive model calculations[4,5] which are based on a dissociation mechanism essentially identical to that described above.

The highly non-Boltzmann distribution of rotational states is consistent with the rotation reflection pinciple for dissociation involving a range of –O–N–O bending and torsional motions in the initial state (S_0) and a strongly repulsive upper state.[51,52] The principle indicates that specific rotational and vibrational states of photoproducts originate from specific geometries of the ground state parent. The spin–orbit, Λ-doublet states have the same distribution of rotational states, but not the same relative populations. The favored dissociation exit channel is via the $F_1\Pi_{A'}$ state, wherein the single electron $p\pi$ orbital is in the NO plane of rotation. The $F_1\Pi_{A'}$ state is preferentially populated by a factor of ~ 1.4 over the other three channels.

The alignment of the NO fragment, as obtained from the CDAD data, is at the theoretical limit for both the F_1 and F_2 states; the experimental value for the alignment parameter is $\mathscr{A}_0^{(2)} = -0.45 \pm 0.04$. These results indicate that the angular momentum vector $\mathbf{J}$ is perpendicular to the photolysis transition dipole moment μ_p; i.e., the $\mathbf{J}$–μ correlation angle η is 90°.

Additional vector correlations, between $\mathbf{v}$ and μ_p, and between $\mathbf{J}$ and $\mathbf{v}$, substantiate an overall planar dissociation process with the transition dipole moment μ_p lying in the plane and with a $\mathbf{v} \angle \mu_p$ angle (ρ) in the range of 13° to 24°. The $\mathbf{v}$–$\mathbf{J}$ correlation varies for each final state and smaller values for χ ($\mathbf{v} \angle \mathbf{J}$) are interpreted as resulting from out-of-plane and bending motions of the –NO group in the parent ground state ("reflection principle") or from induced "twist" in the dissociation surface (S_2) leading to specific final states.

This study demonstrates the utility of REMPI techniques in determining detailed features of photodissociation dynamics. The CDAD technique offers a straightforward means of obtaining initial state alignment. The angular distribution of REMPI photoions, coupled with CDAD provide a rather direct description of the angular correlation

between the photolysis transition dipole moment, the photofragment angular momentum and fragment velocity. The advantages offered by these methods include wide applicability of REMPI to molecular systems, relative simplicity of the experimental setup, and a clear-cut data reduction scheme.

ACKNOWLEDGMENTS

J.W.W. and M.G.W. would like to thank Dr. Greg Hall for helpful discussions. The research at Brookhaven National Laboratory was supported under Contract No. DE-AC02-76CH00016 with the U.S. Department of Energy and by its Division of Chemical Sciences, Office of Basic Energy Sciences. Work at the California Institute of Technology was supported by grants from the National Science Foundation (CHE-8521391), Air Force Office of Scientific Research (Contract No. 87-0039), and the Office of Health and Environmental Research of the U.S. Department of Energy (DE-FG03-87ER60513). R.L.D. and V.M. also acknowledge the use of the resources of the San Diego Super Computer Center, which is supported by the National Science Foundation.

APPENDIX

This section provides a classical derivation of photoion angular distributions resulting from one-photon dissociation followed by a 1 + 1 REMPI probe of the fragment. It is assumed that the dissociation is instantaneous such that the angular distribution reflects the angular relation between the vector quantities μ_p, **J**, and **v** immediately after photolysis; these quantities were defined in Sec. III C. The derivation will provide expressions for the b_0, b_2, and b_4 parameters of Eq. (20) in terms of the angles ρ ($\mu_p \angle \mathbf{v}$), χ(**J**$\angle$**v**), and η($\mu_p \angle \mathbf{J}$). In this derivation it is assumed that the angular distributions characterized by ρ, χ, and η are for fixed values of these three angles, and do not include a distribution for each angle. However, it is reasonable to expect that photofragments in specific final states will be produced with a range of values in these angles. Therefore, it is more appropriate to interpret any set of [ρ, χ, η] extracted from experimental data by this procedure as representing an average of each angle over a distribution.

Figure 8 defines two coordinate systems which are relevant to this discussion. The top half of the figure defines coordinatesabout the center-of-mass of the dissociating system; the photolysis (ϵ_p) and fragment absorption (ϵ_a) electric vectors are parallel and along the z axis. The photoions are detected along the velocity vector (of a photofragment) **v** at angle θ. [The symmetry of the system makes the azximuthal angle ϕ a trivial variable, i.e., $I(\theta; \rho, \chi, \eta)$ and all quantities employed in deriving it do not depend on ϕ.] The lower half of the figure depicts a coordinate system in relation to **v**, the axis of detection, about which we define the directions of μ_p and **J** in terms of the angles (ρ, ϕ'') and (χ, ϕ'), respectively. The requirement that η remain fixed imposes a fixed relation between the azimuthal angles ϕ'' and ϕ'. Integration about either of ϕ'' or ϕ' averages over all possible orientations of the parent molecule.

The photolysis (parent excitation) probability $|\mu_p \cdot \epsilon_p|^2$,

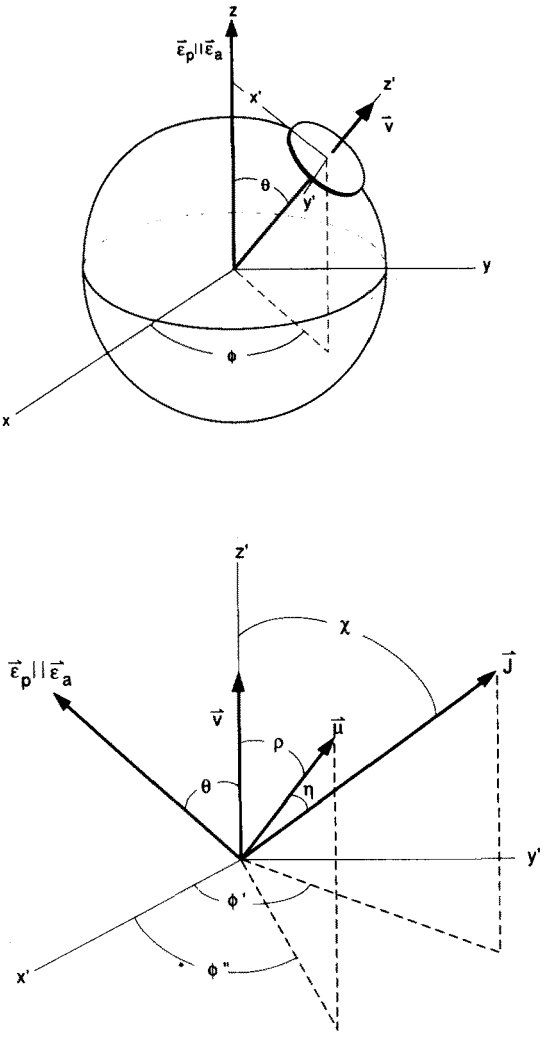

FIG. 8. Vector correlation system. See the text for a description.

is proportional to $k_p \equiv \cos^2 \omega$, where ω is the angle between μ_p and ϵ_p. Then ω is related to ρ and θ by

$$\cos \omega = \cos \rho \cos \theta + \sin \rho \sin \theta \cos \phi''. \quad \text{(A1)}$$

If ϕ' is uncorrelated to ϕ'', due to either photolysis mechanism or detection scheme, then the photofragment angular distribution can be obtained by integration of k_p [the square of Eq. (A1)] about ϕ'' to yield the well known expression $I(\theta) \propto 1 + \beta P_2(\cos \theta)$, where the parameter β is defined as $\beta \equiv 2P_2(\cos \rho)$.

However, if the photofragment detection probability depends on the relative orientation of **J** with respect to the probe light polarization ϵ_a, then a correlation exists between ϕ'' and ϕ'. For a one-photon excitation, the transition probability is proportional to k_a, which is given by

$$k_a \propto E \begin{pmatrix} J + \Delta J & 1 & J \\ M_J & 0 & M_J \end{pmatrix}^2, \quad \text{(A2)}$$

where E are the Earls intensities described in Sec. III A, $(\cdots)$ are 3-j symbols, and ΔJ is -1, 0, and $+1$ for P, Q, and R branch transitions, respectively. The M_J values are the projections of J onto the quantization axis defined by ϵ_p, such that

$$M_J = J\cos\alpha,$$

The angle α is between ϵ_p and **J**, and is given in terms of the angles in the coordinate system of Fig. 8:

$$\cos\alpha = \sin\chi\sin\theta\cos\phi' + \cos\chi\cos\theta. \tag{A3}$$

Equation (A2) can be rewritten by substituting explicit expressions for the 3-*j* symbols:

$$k_a(P\text{ branch}) = E\frac{J}{(2J+1)(2J-1)}\sin^2\alpha, \tag{A4}$$

$$k_a(Q\text{ branch}) = E\frac{J}{(2J+1)(J+1)}\cos^2\alpha, \tag{A5}$$

$$k_a(R\text{ branch}) = E\frac{J^2}{(2J+1)(2J+3)(J+1)} \times[\sin^2\alpha + 2/J + 1/J^2]. \tag{A6}$$

The angle between **J** and μ_p, η, imposes a restriction of ϕ' and ϕ'', which is obtained from

$$\cos\eta = \frac{\mathbf{J}\cdot\boldsymbol{\mu}_p}{|J|\,|\mu_p|} = \sin\chi\sin\rho\cos(\phi'-\phi'') + \cos\chi\cos\rho \tag{A7}$$

to yield

$$\cos(\phi'-\phi'') = \frac{\cos\eta - \cos\chi\cos\rho}{\sin\chi\sin\rho}. \tag{A8}$$

We can then rewrite Eq. (A1):

$$\cos\omega = \cos\rho\cos\theta + \sin\rho\sin\theta\cos(\phi'-\phi'')\cos\phi' + \sin\rho\sin\theta\sin(\phi'-\phi'')\sin\phi'. \tag{A9}$$

The angles χ,ρ, and η are not completely independent of each other. In fact, given any two, the third must be greater than the difference and less than the sum of the first two:

for a given χ and ρ: $|\chi-\rho|\leqslant\eta\leqslant(\chi+\rho)$,

for a given ρ and η: $|\rho-\eta|\leqslant\chi\leqslant(\rho+\eta)$,

for a given η and χ: $|\eta-\chi|\leqslant\rho\leqslant(\eta+\chi)$.

The photoion angular distribution is then the integral over ϕ' of the product of k_p [the square of Eq. (A9)] and k_a [Eqs. (A4)–(A6)],

$$I(\theta;\rho,\chi,\eta) \propto \int_0^{2\pi} k_p k_a\, d\phi' = \int_0^{2\pi}[\cos^2\omega][F\cdot(h\cos^2\alpha+g)]d\phi', \tag{A10}$$

where F is the $Ef(J)$ term of Eqs. (A4) and (A5); $g=1$ (P branch), 0 (Q branch), and $[1+2/J+1/J^2]$ (R branch); and $h=-1$ for P and R branches and $h=+1$ for Q. The integral is solved analytically by substituting Eqs. (A3) and (A9) into Eq. (A10).

The final result can be regrouped in powers of $\cos\theta$ and recast in Legendre polynomials:

$$I(\theta;\rho,\chi,\eta) \propto b_0[\rho,\chi,\eta] + b_2[\rho,\chi,\eta]P_2(\cos\theta) + b_4[\rho,\chi,\eta]P_4(\cos\theta). \tag{A11}$$

The b_l $[\rho,\chi,\eta]$ are as follows:

$$b_0 = \pm F\{-\cos\eta\cos\chi\cos\rho(2+\tfrac{1}{5}\cos\chi) + \tfrac{31}{30}\cos^2\eta - \tfrac{1}{3}\cos^2\rho + 2\cos^2\rho\cos^2\chi - \tfrac{2}{15}\cos^2\chi - \tfrac{2}{15}\sin^2\rho\sin^2\chi + \tfrac{1}{5}\cos^2\rho\sin^2\rho\} + F\frac{y}{3}(4\sin^2\rho - 2\cos^2\rho), \tag{A12}$$

$$b_2 = \pm F\tfrac{1}{7}\{4\cos\eta\cos\chi\cos\rho(\cos\chi+2) + \tfrac{4}{3}\cos^2\chi + \tfrac{2}{3}\sin^2\rho\sin^2\chi - \tfrac{26}{3}\cos^2\eta - \cos^2\rho(18\cos^2\chi - 4\sin^2\chi)\} + F\frac{2y}{3}(2\cos^2\rho - \sin^2\rho), \tag{A13}$$

$$b_4 = \pm F\tfrac{8}{35}\{\cos\eta\cos\chi\cos\rho(\cos\chi-5) + \tfrac{1}{2}\cos^2\eta - \cos^2\chi + \tfrac{1}{4}\cos^2\rho(7\cos 2\chi+3) + \tfrac{1}{4}\sin^2\rho\sin^2\chi\}, \tag{A14}$$

where the "+" is for P and R branches, and the "−" is for Q branches. The term y is branch dependent: $y=1$ (P), 0 (Q), $(1+1/J)^2$ (R).

The above expressions do not include the angular dependence of the ionization, which is expected to be small[22,38] where the ionization light polarization is at angle θ_i from the excitation or photolysis light. If θ_i is constant and does not change with θ, or if the ionization light is circularly polarized then the ionization has no dependence on θ.

[1] H. Reisler, M. Noble, and C. Wittig, in *Molecular Photodissociation Dynamics*, edited by M. N. R. Ashfold and J. E. Baggott (The Royal Society of Chemistry, London, 1987), p. 139–176.
[2] R. Vasudev, R. N. Zare, and R. N. Dixon, Chem. Phys. Lett. **96**, 399 (1983).
[3] R. Vasudev, R. N. Zare, and R. N. Dixon, J. Chem. Phys. **80**, 4863 (1984).
[4] B. A. Keller, P. Felder, and J. R. Huber, Chem. Phys. Lett. **124**, 135 (1986).
[5] B. A. Keller, P. Felder, and J. R. Huber, J. Phys. Chem. **91**, 1114 (1987).
[6] U. Brühlmann, M. Dubs, and J. R. Huber, J. Chem. Phys. **86**, 1249 (1987).
[7] M. Dubs, U. Brühlmann, and J. R. Huber, J. Chem. Phys. **84**, 3106 (1986).
[8] F. Lahmani, C. Lardeux, M. Lavollée, and D. Solgadi, J. Chem. Phys. **73**, 1187 (1980).
[9] F. Lahmani, C. Lardeux, and D. Solgadi, J. Chem. Phys. **73**, 4433 (1980).
[10] F. Lahmani, C. Lardeux, and D. Solgadi, Chem. Phys. Lett. **102**, 523 (1983).
[11] F. Lahmani, C. Lardeux, and D. Solgadi, Chem. Phys. Lett. **129**, 24 (1986).
[12] O. Benoist D'Azy, F. Lahmani, C. Lardeux, and D. Solgadi, Chem. Phys. **94**, 247 (1985).
[13] G. Inoue, M. Kawasaki, H. Sato, T. Kikuchi, S. Kobayashi, and T. Arikawa, J. Chem. Phys. **87**, 5722 (1987).
[14] T. Ebata, H. Yanagishita, K. Obi, and I. Tanaka, J. Chem. Phys. **69**, 27 (1982).
[15] A. F. Tuck, J. Chem. Soc. Faraday Trans. 2 **73**, 689 (1977).
[16] D. Schwartz-Lavi, I. Bar, and S. Rosenwaks, Chem. Phys. Lett. **128**, 123 (1986).
[17] D. Schwartz-Lavi and S. Rosenwaks, J. Chem. Phys. **88**, 6922 (1988).
[18] C. H. Greene and R. N. Zare, J. Chem. Phys. **78**, 6741 (1983).
[19] R. N. Dixon, J. Chem. Phys. **85**, 1866 (1986).
[20] G. E. Hall, N. Sivakumar, D. Chawla, and P. L. Houston, J. Chem. Phys. **88**, 3682 (1988).
[21] D. C. Jacobs and R. N. Zare, J. Chem. Phys. **85**, 5457 (1986).
[22] D. C. Jacobs, R. J. Madix, and R. N. Zare, J. Chem. Phys. **85**, 5469 (1986).
[23] R. L. Dubs, S. N. Dixit, and V. McKoy, J. Chem. Phys. **85**, 656 (1986).

[24]R. L. Dubs, S. N. Dixit, and V. McKoy, J. Chem. Phys. **85**, 6267 (1986).
[25]R. L. Dubs, V. McKoy, and S. N. Dixit, J. Chem. Phys. **88**, 968 (1988).
[26]R. L. Dubs, S. N. Dixit, and V. McKoy, Phys. Rev. Lett. **54**, 1249 (1985).
[27]R. L. Dubs, S. N. Dixit, and V. McKoy, J. Chem. Phys. **86**, 5886 (1987).
[28]R. L. Dubs, S. N. Dixit, and V. McKoy, Phys. Rev. B **32**, 8389 (1985).
[29]J. R. Appling, M. G. White, R. L. Dubs, S. N. Dixit, and V. McKoy, J. Chem. Phys. **87**, 6927 (1987).
[30]J. R. Appling, M. G. White, W. J. Kessler, R. Fernandez, and E. D. Poliakoff, J. Chem. Phys. **88**, 2300 (1988).
[31]N. Sanders, J. E. Butler, L. R. Pasternack, and J. R. McDonald, Chem. Phys. **48**, 203 (1980).
[32]I. Nenner and J. A. Beswick, in *Handbook on Synchrotron Radiation, Vol. II*, edited by G. V. Marr (North-Holland, Amsterdam, 1986).
[33]W. C. Wiley and I. H. McLaren, Rev. Sci. Instrum. **73**, 4816 (1955).
[34]R. Ogorzalek-Loo, G. E. Hall, H.-P. Haerri, and P. L. Houston, J. Phys. Chem. **92**, 5 (1988).
[35]R. N. Zare, Ber. Bunsenges. Phys. Chem. **86**, 422 (1982).
[36]C. H. Greene and R. N. Zare, Annu. Rev. Phys. Chem. **33**, 119 (1982).
[37]In Ref. 25 a factor of

$$(-1)^{L+L'}\left\{\frac{(2L+1)(2L'+1)}{4\pi}\right\}^{1/2}\begin{pmatrix} L & L' & \mathbf{L} \\ 0 & 0 & 0 \end{pmatrix}$$

should be included on the right-hand side of Eq. (26) for $\beta_{\mathbf{L}}$. See also the left-hand side of Eq. 1.2-33 of M. Weissbluth, *Atoms and Molecules* (Academic, New York, 1978).
[38]R. L. Dubs (unpublished results).
[39]Table I of Ref. 25 does not explicitly give an expression for C_{20}, but it can be easily obtained from C_{02} and the symmetry properties of Eq. (6) of that reference.
[40]While this independent experiment can be performed on a gas phase sample of NO, it might not be possible for an unstable photofragment.
[41]L. T. Earls, Phys. Rev. **48**, 423 (1935).
[42]J. W. Keller, W. T. Hill III, D. L. Ederer, T. J. Gil, and P. W. Langhoff, J. Chem. Phys. **87**, 3299 (1987).
[43]M. E. Rose, Phys. Rev. **91**, 610 (1953).
[44]M. Tanaka, J. Tanaka, and S. Nagakura, Bull. Chem. Soc. Jpn. **39**, 766 (1966).
[45]P. Tarte, J. Chem. Phys. **20**, 1570 (1952).
[46]G. Herzberg, *Molecular Spectra and Molecular Structure, I. Spectra of Diatomic Molecules* (Van Nostrand, New York, 1950), pp. 218–240, 257–264.
[47]K. P. Huber and G. Herzberg, *Molecular Spectra and Molecular Structure, IV. Constants of Diatomic Molecules* (Van Nostrand, New York, 1979), pp. 468–481.
[48]M. H. Alexander, P. Andresen, R. Bacis, R. Bersohn, F. J. Comes, P. J. Dagdigian, R. N. Dixon, R. W. Field, G. W. Flynn, K.-H. Gericke, E. R. Grant, B. J. Howard, J. R. Huber, D. S. King, J. L. Kinsey, K. Kleinermanns, K. Kuchitsu, A. C. Luntz, A. J. McCaffery, B. Pouilly, H. Reisler, S. Rosenwaks, E. W. Rothe, M. Shapiro, J. P. Simons, R. Vasudev, J. R. Wiesenfeld, C. Wittig, and R. N. Zare, J. Chem. Phys. **89**, 1749 (1988).
[49]F. Lahmani, C. Lardeux, and D. Solgadi, J. Chem. Phys. **77**, 275 (1982).
[50]M. A. O'Halloran, Faraday Discuss. Chem. Soc. **82**, 38 (1986).
[51]R. Schinke, J. Chem. Phys. **85**, 5049 (1986).
[52]R. Schinke and V. Engel, Faraday Discuss. Chem. Soc. **82**, 111 (1986).
[53]P. Shokoochi, S. Hay, and C. Wittig, Chem. Phys. **110**, 1 (1984).
[54]H. Joswig, M. A. O'Halloran, R. N. Zare, and M. S. Child, Faraday Discuss. Chem. Soc. **82**, 79 (1986).
[55]G. E. Busch and K. R. Wilson, J. Chem. Phys. **56**, 3626, 3638, 3655 (1972).